Range-Finding SPAD Array With Smart Laser-Spot Tracking and TDC Sharing for Background Suppression

**VINCENZO SESTA [ID] [1], KLAUS PASQUINELLI [ID] [1], RENATO FEDERICO [1,2],
FRANCO ZAPPA [ID] [1] (Senior Member, IEEE), AND FEDERICA VILLA [ID] [1] (Member, IEEE)**

1 Dipartimento di Elettronica, Informazione e Bioingegneria, Politecnico di Milano, 20133 Milano, Italy
2 Flash Research and Development Division, SK Hynix Italy S.r.l., 28064 Agrate Brianza, Italy

CORRESPONDING AUTHOR: V. SESTA (e-mail: vincenzo.sesta@polimi.it)

ABSTRACT We present the design and experimental characterization of a CMOS sensor based on Single-Photon Avalanche Diodes for direct Time-Of-Flight single-point distance ranging, under high background illumination for short-range applications. The sensing area has a rectangular shape (40×10 SPADs) to deal with the backscattered light spot displacement across the detector, dependent on target distance, due to the non-confocal optical setup. Since only few SPADs are illuminated by the laser spot, we implemented a smart laser-spot tracking within the active area, so to define the specific Region-Of-Interest (ROI) with only SPADs hit by signal photons and a smart sharing of the timing electronics, so to significantly improve Signal-to-Noise Ratio (SNR) of TOF measurements and to reduce overall chip area and power consumption. The timing electronics consists of 80 Time-to-Digital Converter (TDC) shared among the 400 SPADs with a self-reconfigurable routing, which dynamically connects the SPADs within the ROI to the available TDCs. The latter have 78 ps resolution and 20 ns Full-Scale Range (FSR), i.e., up to 2 m maximum distance range. An on-chip histogram builder block accumulates TDC conversions so to provide the final TOF histogram. We achieve a precision better than 2.3 mm at 1 m distance and 80% target reflectivity, with 3 klux halogen lamp background illumination and 2 kHz measurement rate. The sensor rejects 10 klux of background light, still with a precision better than 20 mm at 2 m.

INDEX TERMS Light detection and ranging (LiDAR), laser rangefinder, time-of-flight (TOF), time-to-digital converter (TDC), single photon avalanche diode (SPAD), background light rejection.

I. INTRODUCTION

LIGHT Detection and Ranging (LiDAR) is a widespread technique for 3D ranging and distance measurements and has many applications in automated systems interacting with the external environment, e.g., in industrial and security environments [1]–[5]. Silicon Single-Photon Avalanche Diodes (SPADs) are solid-state detectors capable of single-photon sensitivity in the visible and near-infrared spectrum that can be manufactured in CMOS processes together with on-chip analog or digital circuitry, to devise rugged, low-cost and monolithic imagers [6]. SPADs are the best candidates for direct Time-of-Flight (TOF) and Time-Correlated Single-Photon Counting (TCSPC) applications [7]. As in TCSPC, also for 3D ranging the photon arrival times measured after a sufficient number of pulsed laser shots can be accumulated

into a histogram, so to accurately estimate the distance by means of the histogram centroid (or further postprocessing) even in presence of very high background light [8]–[10]. In many cases, the spot signal does not cover the whole sensing area of the array detector, but only few pixels. In this situation many TOF measurements are useless, being mostly due to background photons, while only few of them are useful, being given by photons of the laser return. This comes with the double effect of increased noise baseline in the histogram and a waste of area, power consumption, and data processing for all TOF measurements triggered outside the signal spot.

Various architectures have been proposed to face these issues [11]–[23], e.g., by exploiting temporal and spatial coincidence to perform TOF acquisitions for only those

pixels effectively triggered by the laser spot, thus allowing to share on-chip resources and reduce data throughput. The coincidence is usually performed through macropixels composed by more than one SPAD, whose output triggers the time conversion circuitry only if a minimum number of SPADs got triggered by photons within a fixed coincidence time window, typically corresponding to the laser pulse width. In that way, macropixels trigger a Time-to-Digital Converter (TDC) even if some SPADs got triggered by background events and only a few (or none) detected a laser photon. Alternative solutions employ a Silicon Photomultiplier (SiPM), which is composed by many SPADs all connected in parallel and acting as one overall analog detector. In that way, the SiPM is sensitive to multi-photons hitting the active area either at different time instants or even concurrently, because each SPAD acts as an independent single-photon detector. Therefore, SiPM are particularly suited for background rejection, by setting a coincidence threshold at the analog output [22], [23].

However, solutions based on time coincidence have a main drawback: the higher the number of SPADs triggering the same TDC, the more the information loss. The reason being that many photons detected by different SPADs provide just one TOF data, thus degrading target's distance precision computed through the histogram centroid. Also, the proper coincidence threshold is very critical to set, since it has to be sufficiently high to reject background, but without losing signal events.

Starting from a previous theoretical study [21], in this work we illustrate the design and characterization of a 40×10 single-point direct TOF sensor, showing a precision better than 2.3 mm at 1 m for an 80% reflectivity target with 3 klux background. The architecture allows to identify those SPADs actually illuminated by the signal photons due to the laser spot from those SPADs triggered by uncorrelated background photons, by means of a smart Region-Of-Interest (ROI) detection and to optimize the timing electronics by a smart sharing of the TDC electronics [24], [25]. The proposed architecture overcomes the main drawbacks of the time coincidence-based approaches because each detected signal photon is individually time-stamped, thus maximizing data collection and measurement precision. In fact, as we theoretically estimated in [21], 500 TOF acquisitions are enough to achieve an accuracy better than 10 mm with 3 klux background, using a 670 nm pulsed laser with 100 mW peak power, 1 MHz repetition rate, and width shorter than 3 ns Full Width at Half Maximum (FWHM).

The proposed ROI-based approach has some limitations due to the dependence on signal and background levels, as reported in [21], and when targets move with a transverse velocity higher than 4 m/s, since some frames could be partially lost because the ROI selection is based on the previous 500 laser pulses. Furthermore, such ROI-based approach suits single-spot measurements and not imaging, unlike time-based coincidence solutions.
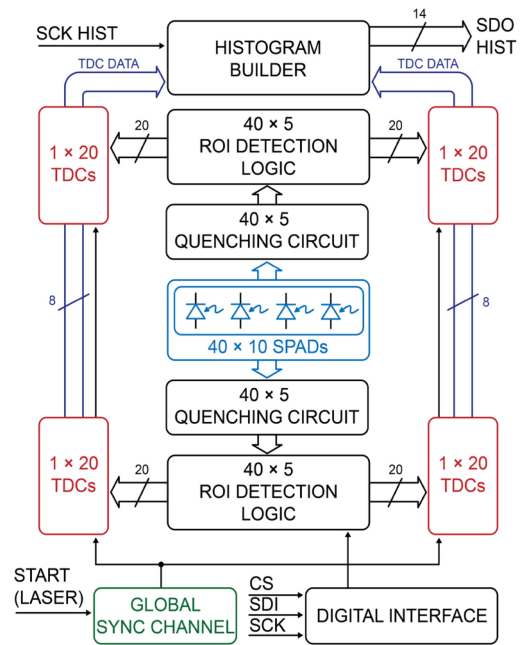

FIGURE 1. Block diagram of the chip, with the main building blocks: 40×10 SPADs with quenching circuits, ROI selection logic, 80 TDCs, histogram builder and input/output digital interface.

Section II describes the array architecture, Section III the experimental results, and Section IV draws the conclusions.

II. ARRAY ARCHITECTURE

Fig. 1 shows the block diagram of the chip, fabricated in a 160 nm CMOS technology [26]. The chip consisting of 40×10 SPADs with quenching circuits, ROI detection logic, 80 TDCs, a histogram builder and a digital input/output interface. To maximize fill-factor and number of pixels within the laser spot, we assembled the SPADs with no electronics in the between. The chip size is 2.73×3.37 mm^2 and the sensing area occupies the chip center as shown in Fig. 2. Given an expected spot size of about 150 μm diameter (see also [21]), the overall active area has a height of 248 μm (so to allow a slight vertical displacement of the spot) and a length of 950 μm (to enable a wider horizontal displacement due to the different distance of the target object, in the considered non-confocal optical setup), constituted by 400 square SPADs with rounded corners (about 82 μm^2 active area). The resulting fill-factor is 14%. The quenching circuits are laid out in two 40×5 arrays along the long sides of the array. Each quenching circuit is connected to the corresponding ROI detection circuitry. Each TDC is shared among five SPADs, so eighty TDCs are implemented in each row, and they are divided in four banks of 20 TDCs each. This configuration of TDC sharing aims at optimizing chip area and power consumption and, at the same time, to best accommodate the laser spot, without losing useful conversions.

When a photon hits a SPAD, the quenching circuit senses the avalanche current and generates a digital pulse for the
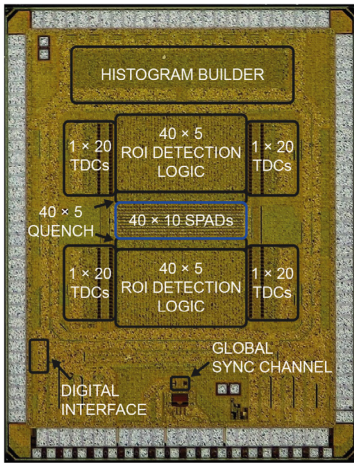
FIGURE 2. Chip micrograph with highlighted the main building blocks. The chip size is 2.73 mm × 3.37 mm, and the sensing area (highlight in blue) occupies the center of chip.

ROI selection circuit. After the ROI detection is performed (see the following Section II-B), only SPADs inside the ROI are enabled to trigger the shared TDCs, providing 78 ps resolution and 20 ns Full-Scale range (FSR).

The chip also includes a histogram builder block to collect all TOF measurements; whereas the target distance is evaluated by means of centroid computation, to be performed off-chip through external processing. Each block of the proposed array is described in detail in the following sections.

A. SPAD QUENCHING CIRCUIT

SPADs are able to detect photons only when biased above their breakdown voltage; the difference between the applied bias and the breakdown voltage is called excess bias, V_{EX}. We employed a Variable-Load Quenching Circuit topology [27], [28] to sense the avalanche and then quench the SPAD below the breakdown voltage, to minimize the avalanche current while using a low number of transistors. The circuit makes use of thick-oxide transistors for sensing, quenching, and resetting the SPAD, allowing up to 5 V excess bias operation, in combination with low voltage (1.8 V) transistors to reduce area occupation. Layout was optimized to match the VLQC pitch with the SPAD one (24 μm) and to have comparable parasitism between different anodes. SPAD detectors are activated only within precise time window, set equal to the TDC full-scale range. The quenching circuit (see Fig. 3) provides prompt avalanche quenching and fast detector reset (< 1 ns fall transitions of the anode voltage between 80% - 20%) even with the non-negligible parasitic capacitance of the long metal lines.

Fig. 4 shows the working operation of the described VLQC. When the SPAD is ready to detect photons, the transistor M2 (with small form-factor) is on while M1 (with large form-factor) is off, so that the ignited avalanche current increases the SPAD anode voltage and turns slightly on
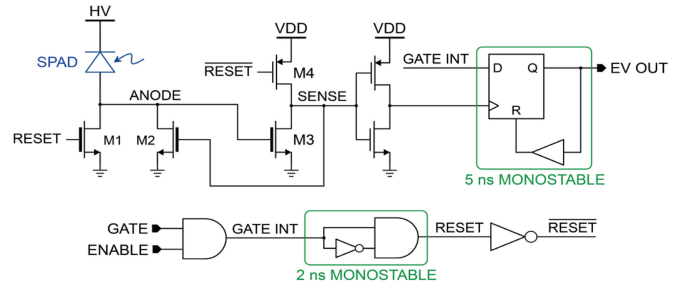

FIGURE 3. Simplified schematics of the quenching circuit. High voltage (5V) transistors are drawn with a thicker gate.
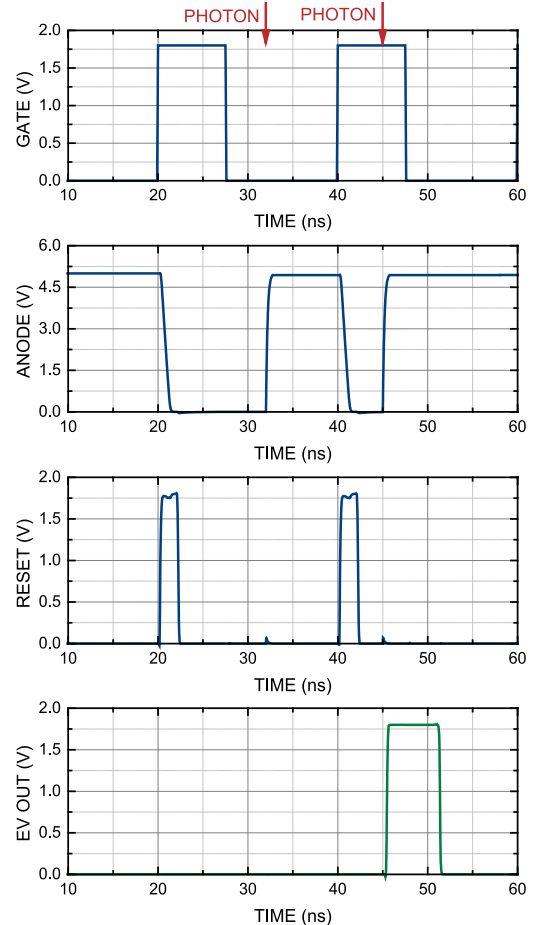

FIGURE 4. Simulated timing diagrams of the VLQC. The EV OUT is generated only if the photon is detected within the acquisition (GATE) window.

transistor M3, which pulls the SENSE node voltage down, thus turning M2 off and speeding up quenching. The 5 ns output pulse (EV OUT) is generated through a monostable only when triggering happened within the gate window. After each photon detection, the SPAD remains below breakdown until a new gate window is applied: M1 resets the SPAD and M4 resets the SENSE node. In fact, on the rising edge of gate signal, the reset transistor M1 is active for about 2 ns to quickly bring the SPAD above breakdown. This "soft" gating approach (EV OUT generated only

during the gate-on window, so to mask ignitions outside the detection window) greatly reduces dynamic power consumption in respect to "hard" gating operations, i.e., when the SPAD is enabled above breakdown or disabled below breakdown, so to actively apply large voltage transitions to the SPAD's anode, thus charging and discharging the junction's capacitance. Moreover, the "soft" gating requires neither an active PMOS transistor to disable the SPAD by pulling the anode voltage up to a voltage equal to or higher than the excess bias of the SPAD, nor such a new supply rail.

Eventually, an ENABLE signal, provided through a distributed shift register, is used to either enable or shut down each SPAD, which cannot be rearmed at the gate signal rising edge: in this way it is possible to disable "hot" SPADs, i.e., SPADs with too high Dark Count Rate (DCR) or to anyhow limit the number of SPADs in operation.

B. ROI DETECTION LOGIC

In single point ranging, only few SPADs are covered by the laser spot, thus we implemented an innovative smart Region-Of-Interest (ROI) detection for the laser-spot tracking, in order to minimize the number of TDCs, while still being sensitive to all useful signal photons within the spot, by means of the smart TDC sharing described in [21] and in Section II-C.

The ROI selection idea relies on the fact that back-scattered laser photons trigger the SPADs only during a well-defined temporal window (set equal to the FSR of TDC), whereas background light is uniformly distributed across time. Thus, to ascertain if a SPAD is within the laser spot and consequently within the ROI, we check for each SPAD the difference between photons counted within the window corresponding to the laser return (i.e., with signal photons and background photons) and another window with the same duration but when no signal is expected (i.e., with only background photons), then we compare such a value with a user-defined threshold. In order to implement the photon count difference and comparison, we integrated an up/down digital counter preloaded with the desired N_{TH} threshold value: photons within the expected laser return window are counted downwards, whereas background photons are counted upwards, during a time window with the same duration, but when the laser is off. Fig. 5 shows the timing diagram for the ROI evaluation, during many laser shots. The figure shows an exemplifying case of a generic SPAD #1 within the laser spot and another generic SPAD #2 outside the laser spot. A frame can consist for example of 500 laser shots. At the beginning of each frame, counters are pre-loaded with the positive threshold value N_{TH}; then counters increment by $+1$ anytime a photon is detected when the laser is off and decrement by -1 anytime a photon is detected when the laser is on. Note that within each enabling window (either Up or Down) the counts can increment or decrement at most by 1, because a SPAD can be triggered only once within each
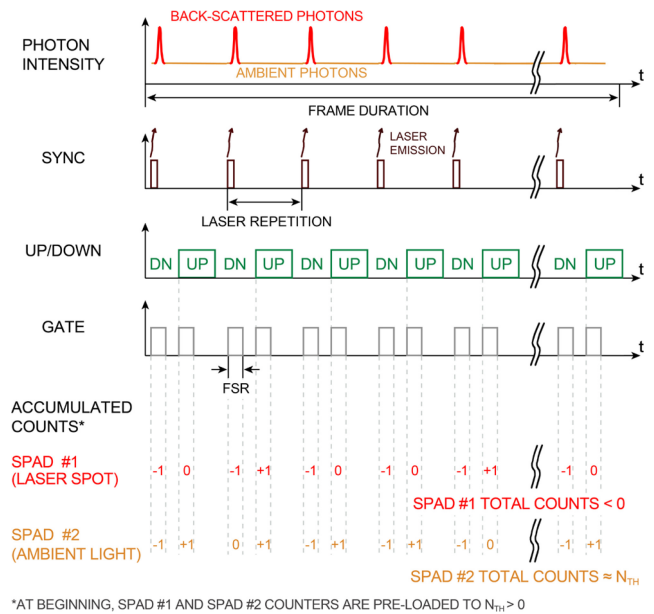

FIGURE 5. Timing diagram to perform ROI selection. During 500 laser shots, counters run downward when signal photons are expected, while upward to count just background photons. For instance, SPAD #1 inside the spot, accumulates a total negative count while SPAD #2 outside the spot, accumulates a positive count near to preloaded threshold value N_{TH}.

enabling window, being reset at the following window. Moreover, since background is almost the same between two subsequent gates, we have the same probability to detect background photons in both upwards and downward windows.

After 500 enabled windows in both upward and downward counting, counters accumulating a negative value (e.g., SPAD #1) signal SPADs within the laser spot, while counters with a final positive value, around the threshold value N_{TH}, (e.g., SPAD #2) are to be considered outside the laser spot. Therefore, all SPADs associated to negative total counts are enabled to trigger the shared TDCs during the following frame. With this implementation, there is no need of digital comparators since the sign bit of each counter suffices to detect if the corresponding SPAD is within the ROI (laser spot) or not.

Fig. 6 shows the simplified block diagram of the ROI detection logic, which includes the 10-bit up/down counter, the logic to pre-load the threshold N_{TH} through serial communication and the sign bit discrimination to selectively connect the active quenching output pulse (EV OUT, see Fig. 3) to the input of shared TDC through an NMOS (M_{OD}), which drives the open-drain shared TDC line, as shows in Fig. 6. The counters' number of bits has been chosen to largely accommodate the possible counts, considering the worst case, e.g., for a frame of 500 cycles with only up (or down) counts, 9 bits would suffice. A saturation logic is also implemented in the counters when the full-scale value is reached, to avoid re-folding, confusing an extremely high negative value as a low positive one and vice versa.
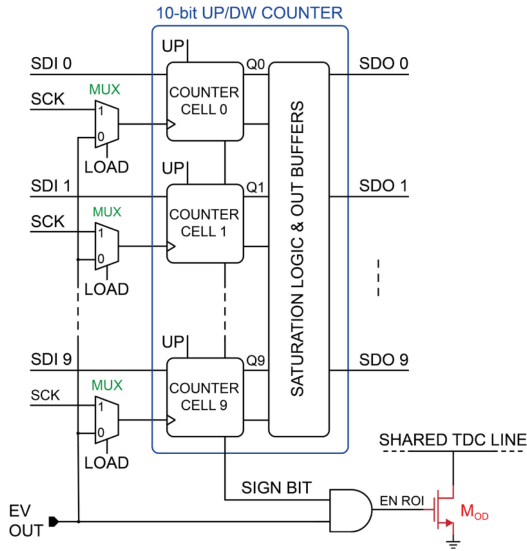
FIGURE 6. Simplified block diagram of the ROI detection logic, based on 10-bit up/down counter per each SPAD. The user-defined threshold is set through a serial communication bus.

In order to pre-load counters with a user-defined value, each up/down counter cell implements a multiplexer, which transforms the counter into a shift register, allowing to load the threshold value through a serial communication bus. The same bus allows to readout the content of all counters for debug purposes or for acquiring intensity maps across the active area.

Since the shared TDC line in Fig. 6 is a very long metal path shared among 5 pixels of the same row, the open drain NMOS (M_{OD}) has been properly sized to guarantee a sharp rising-edge and negligible jitter contribution.

C. SMART TDC SHARING
Due to the smart laser-spot detection, only SPADs within the ROI can trigger the TDC, which measures the photons' TOF. To avoid signal loss, neighboring SPADs, which may be covered by the laser spot, are connected to different TDCs. Therefore, a smart TDC sharing is performed between SPADs belonging to the same row of the array [21].

The number of TDCs per row is chosen to reduce area consumption and to best accommodate the laser while keeping the same number of available TDCs for each row. Considering a spot diameter of 150 μm (see [21]) and the 24 μm SPAD pitch, the maximum number of adjacent columns within the laser spot will never exceed 6.25. Therefore, a reasonable trade-off is to have one TDC every 8 SPADs, so that each TDC is shared between five SPADs, thus minimizing the number of TDCs and maximizing the number of SPADs enabled to ignite a TDC.

Fig. 7 shows the concept applied to one full row of the SPAD array with 40 columns. Following this scheme, each row is then sub-divided into five sectors of eight SPADs each, where all SPADs within the same sector are connected to

a different TDC. To optimize area occupation and guarantee symmetry, the 80 TDCs are divided into four banks of 20 TDCs each, all positioned on the sides of the ROI logic.

Since the shared TDC lines are very long metal paths connecting the open drain NMOS transistors (see Fig. 6), the TDC shared lines have been carefully laid out to minimize delay skew between NMOS transistors. As a result, the skew along the TDC line is not that critical, thus it does not significantly impact distance precision (as it will be shown in Fig. 16).

The implemented TDCs are based on an architecture employing a multiphase clock interpolation based on a Delay-Locked Loop (DLL) [28], [29], which generates 16 clock phases from a 400 MHz reference clock; each of these clock phases is delayed by 78 ps from one another. Each 16 clock phases can be tuned, to compensate any delay mismatch, thus improving the overall TDC linearity. Fig. 8 shows the simplified block diagram of each TDC. This architecture employs a global SYNC channel, which is driven by the laser sync signal (i.e., START signal) and 80 TDC channels, which are triggered by photons detected within the ROI (i.e., STOP signals). Both START and STOP signals are asynchronous with respect to the TDC reference clock, thus implementing the sliding-scale technique and improving conversion linearity [29], [30].

Each TDC channel has a 3-bit counter that counts the number of reference clock periods between START and STOP, ensuring the 20 ns FSR needed to reach the 2 meters maximum distance range, and a 5-bit STOP interpolator, boosting the measurement resolution to 78 ps. The global SYNC channel has only the START interpolator. Each interpolator is made of fast latches, which sample the status of the multiphase clocks at the rising-edge of the input event. To reduce routing complexity and overall power consumption, the interpolators exploit both rising- and falling-edges of the clock phases: in this way, by employing only 16 clock phases we get 32 phases (i.e., 5 bit), the first 16 on rising-edges, the last 16 on the falling-edges. Thus, the final TOF measurement is given by:

$$T_{MEAS} = N_{CTR} \cdot T_{CLK} + \frac{T_{CLK}}{32} \cdot \left(N_{f,STOP} - N_{f,START} \right) \quad (1)$$

where N_{CTR} is the counter code while $N_{f,START}$ and $N_{f,STOP}$ are the START and STOP interpolator codes.

D. HISTOGRAM BUILDER
At the end of every laser shot, the global SYNC channel and all TDCs are readout through tri-state buffers acting on an 8-bit common bus line, controlled by a dedicated logic that feeds the histogram builder to accumulate a histogram of all TOF measurements and provided to output pads for post processing.

The histogram builder employs an 8-bit binary subtractor to perform the STOP-START difference and a decoder and counters to accumulate counts to the appropriated time bin's memory cell. Given the FSR, to perform distance measurement up to 2 m with 78 ps resolution, the histogram has
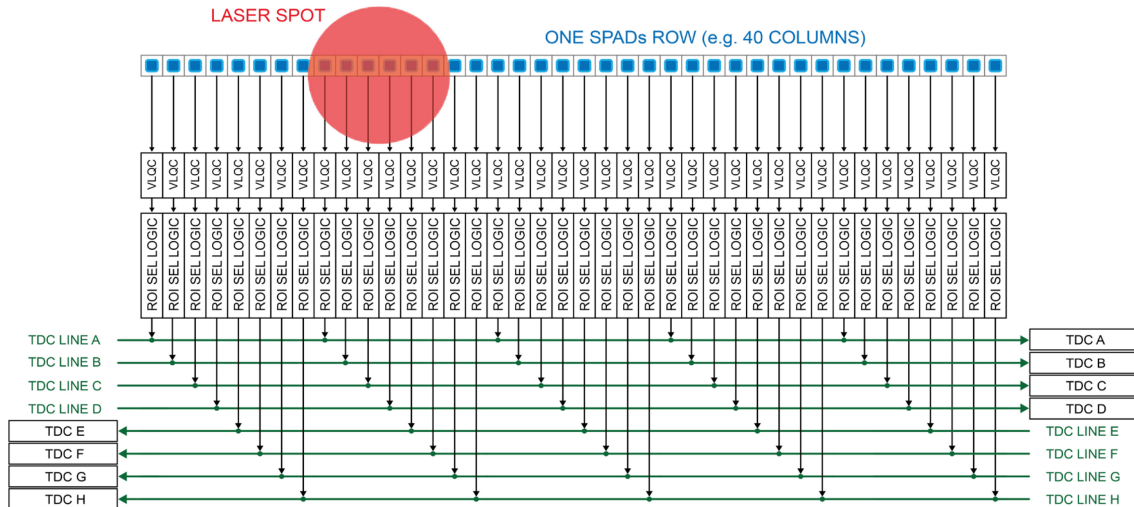
FIGURE 7. TDC sharing performed in one row of the SPAD array: by grouping columns together in 8 channels (from A to H), to fit the expected 150μm laser spot diameter (about 6 SPADs) only 8 TDCs are required per each row whatever is the number of actual columns.
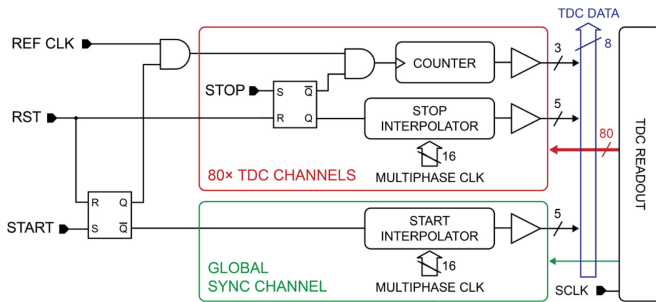

FIGURE 8. Block diagram of one TDC, with the 8-bit output bus for fast readout.

FIGURE 9. Optical setup used for the ROI detection and TOF measurements.

TABLE 1. Parameters of the optical setup used for the measurements.

Element	Parameter	Value
Target	Reflectivity	0.8
Emitter (pulsed laser)	Average power (μW)	140
	Wavelength (nm)	670
	Pulse width, FWHM (ns)	300
Receiver (object lens)	Aperture diameter (mm)	8.57
	Focal length (mm)	12
	N.A.	0.336
	Transmittance	0.9
Receiver (optical filter)	Optical bandwidth (nm)	10
	Transmittance	0.7

allows also to reset the DLL and tune the 16 clock phases, as mentioned before. In addition, the readout of counters is also performed through digital interface to obtain the counts of each pixel and verify the correctness of ROI selection.

The histogram data are readout separately, performing a dedicated serial communication which transfers the data through a 14-bit output bus. Also, the TDC data are readout independently to verify the correctness of TDC conversion and histogram generation. The output data of the 80 TDCs are readout serially through 8-bit output bus, in 810 ns at 100 MHz serial clock. Considering the laser repetition rate specification reported in [21], the TDC readout time is shorter than the 1 μs laser period (1 MHz repetition rate), thus no useful TOF measurements are lost during readout.

been designed to keep 256 time-bins with a 14-bit width for each bin, considering the worst case of all TDC measuring the same TOF in all the 500 samples of a frame.

E. DIGITAL INTERFACE AND READOUT

The array is controlled through a 4-wire communication interface, SPI compatible, and it is used to program the enable for each of the 400 SPAD pixels, as well as, to configure the ROI threshold and bypass values. The digital interface

III. EXPERIMENTAL CHARACTERIZATION

We characterized the single point range-finding SPAD array chip to verify the smart laser-spot tracking (the ROI detection), the shared TDC performance, and the
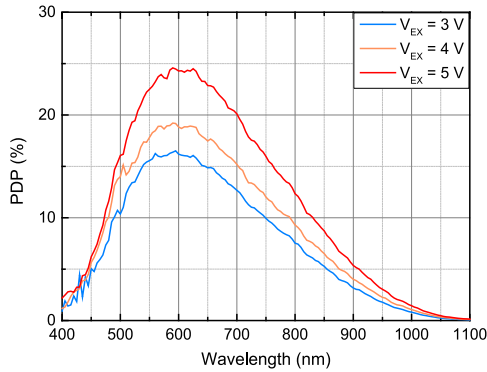
FIGURE 10. Photon Detection Probability (PDP) at different excess bias voltages.

FIGURE 11. Single-shot precision of each TDC (colored curves) and overall precision when adding together the 80 TDCs conversions (black curve) at same delay. The counts of each curve are normalized to the unit area.

performance in terms of distance precision at high background. Fig. 9 shows the optical setup used to verify the ROI detection and to perform TOF measurements. We employed a pulsed laser at 670 nm, with 140 μW average power, 300 ps FWHM, 1 MHz repetition rate, and we mounted a 10-nm-bandwidth optical bandpass filter and single-lens optics onto the chip. Emitter and receiver are placed separately at a distance of about 9 cm, due to the optical setup available in the lab. A halogen lamp illuminates the target to provide the background light up to 10 klux. Table 1 summarizes the optical setup parameters.

First at all, we evaluated the SPAD noise and efficiency and the TDC single-shot precision. Then, we validated the chip functionality by performing TOF measurements at different distances and background illumination levels.

A. SPAD AND TDC PERFORMANCE
We already reported in [26] the detection performance of SPADs we conceived in this 160 nm BCD technology, in terms of Dark Count Rate (DCR), temporal response, and Photon Detection Probability (PDP), the last one being quite important for direct TOF measurements. Fig. 10 shows the measured PDP of the chip at different excess voltages V_{EX}, with a 25% peak at 600 nm with 5V excess voltage. In comparison with the PDP reported in [26], the measured PDP is quite lower due to the small SPAD active area which leads to being more sensitive to the edge effects of SPAD detector. The average DCR is about 800 cps at room temperature and 5 V excess voltage for the 80 μm^2 active area SPADs, corresponding to about 10 cps/μm^2 DCR density. Although quite low, the DCR is not relevant in direct TOF measurements since ambient background is the dominant contribution given the optical setup, 3 klux of ambient light correspond to about 32 Mcps at the SPAD.

Concerning the TDC, we characterized the single-shot precision of all 80 TDCs, by applying external START and STOP signals and by measuring the Full-Width at Half Maximum (FWHM) of the timing-histogram across the whole FSR, varying the delay between START and STOP. The FWHM of single TDC varies between 78 ps (one
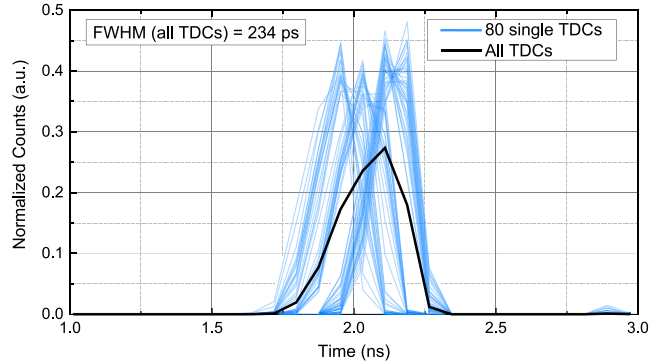
time-bin) to 234 ps with an average of about 168 ps, while the FWHM of all TDCs together is limited between 234 ps to 312 ps with an average of about 269 ps. Fig. 11 shows the single shot precision of each one of the 80 TDCs and the ensemble response, when converting the same START–STOP delay. Four main distributions can be seen, corresponding to the four groups of 20 TDCs each laid out in different positions of the chip (see Fig. 1), which receive slightly different multiphase clocks. The average FWHM of each single TDCs is about 168; when all 80 TDCs are combined together, it increases to 234 ps, mainly due to timing skews among different TDC positions in respect to the multi-phase clocks propagated inside the chip. The correspondingly degraded measurement precision depends on the ROI dimension since a wider laser spot triggers more TDCs, hence time skews among multiphase clocks gets more severe. However, the result does not depend on the position of the ROI within the array, thanks to the smart TDC sharing. In fact, the position of the ROI influence which SPADs can trigger the TDCs, and not which region of the TDCs is activated. Nevertheless, such widening is only about 39% in the worst case (i.e., when all TDCs are triggered) compared to the single pixel's precision (i.e., when only a single TDC is enabled and triggered).

B. ROI DETECTION
We performed some measurements to evaluate the performance of the on-chip ROI detection and the corresponding improvements achieved in the final TOF precision. We acquired 500 μs frames, consisting of 500 gate windows with only background light and other 500 gate windows with background and signal photons. All gate durations were 15 ns (equal to the measurement FSR), which is lower than TDC FSR (equal to 20 ns) since a delay constraint of about 5 ns between START and GATE signal is needed to guarantee the correct operation.

As described in Section II-B and in Fig. 5, a proper digital threshold value must be set into all ROI selection counters before acquisitions. Fig. 12 shows the counts distribution of a SPAD within the laser-spot ROI (i.e., hit by the signal),
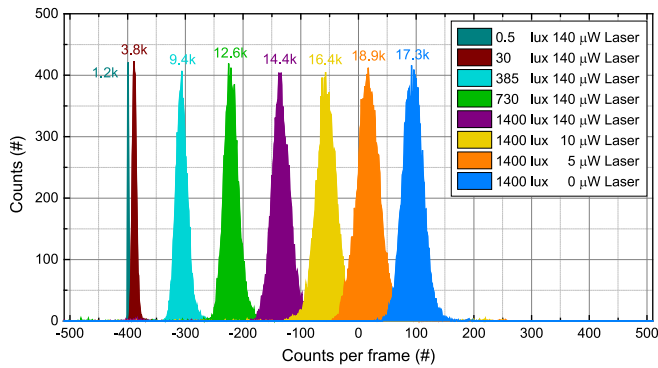
FIGURE 12. Count distributions of a single pixel hit by the signal with a threshold set to 100 in different conditions of signal and background. The total number of detections of each curve is reported above the respective histogram.

FIGURE 13. Ensemble count distributions of all SPADs (top), counts map across the 40 × 10 array (center), and ROI map (bottom) with threshold $N_{TH} = 100$ and 3 klux background light.

with a threshold N_{TH} set to 100. Depending on signal and background levels, each curve is obtained with a different number of detected photons (see the figures at the top of each histogram) in order to reach the same peak count. The blue distribution curve corresponds to an acquisition with no signal, but 1400 lux background: a wide gaussian shape can be easily seen. By increasing laser power and/or decreasing background illumination, the distributions move toward negative counts, since signal photons increment compared to background ones (so the counter decrements more often than when it increments). When background gets negligible compared to signal, the distribution narrows and its centroid moves far away from the set threshold N_{TH}: therefore, the SPAD can be more easily identified to be within the ROI.

Note that the proposed smart ROI detection method has an important advantage: the counting result is independent of the color of the objects, because the threshold value N_{TH} depends only on average background and signal intensities, related to the pulse width of the laser pulse.

Fig. 13 shows the cumulative counts distribution of all SPADs at 3 klux of background light (top) and the corresponding counts and ROI map (center and bottom), with a threshold $N_{TH} = 100$. After a frame with 500 laser shots, two different peaks can be seen: one related to SPADs outside the laser spot, showing positive counts (at around the preloaded threshold +100) and another one related to SPADs inside the laser spot, showing negative counts (at around −150). SPADs with a resulting positive count are considered outside the ROI while those with a resulting negative count are inside the ROI. The TOF measurements accuracy improves if TDC conversions are triggered just by signal photons and not by background ones. In the operating conditions of Fig. 13, with 3 klux background and threshold N_{TH} set to 100, the two peaks intersect at a final count of about −75. Therefore, TOF measurements would improve by moving the intersection of the two peaks towards zero, i.e., by increasing N_{TH} to +175 instead of +100. In that way, the signal-to-noise ratio of the final distance measurement
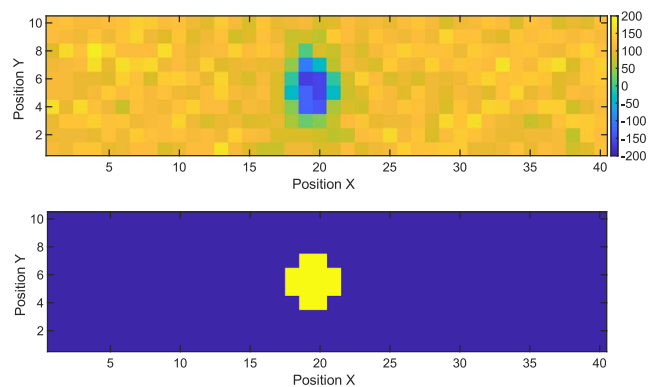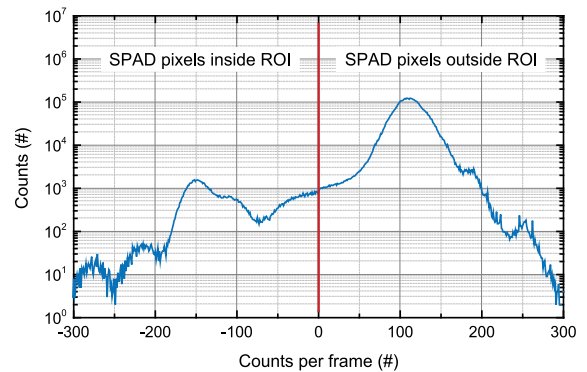
can be improved. This is simply achieved by adjusting the preloaded counter threshold: in the case of Fig. 13, N_{TH} should be increased.

This optimization is valid if operating conditions in terms of target reflectivity and background light remain almost constant during the frame (i.e., for about 500 μs with 500 gate windows and 1 MHz laser). Faster changes would require shorter frames and/or real-time N_{TH} adjustments, by reading out the ROI map (see Fig. 13, bottom) until its dimensions fit the expected laser spot ones.

Fig. 14 compares the TOF histograms accumulated with ROI detection on ($N_{TH} = 80$) and off ($N_{TH} = 1$, so most of 400 SPAD pixels are considered in ROI). The corresponding ROI detection maps shown in Fig. 15 were acquired with the optical setup described in Fig. 9, after one frame (i.e., 500 laser shots at 1 MHz). In case of ROI detection on, we obtained a total of about 2,200 detections since only 5 TDCs got triggered through the ROI selection as showed in Fig. 15. Instead, while when the ROI detection was off ($N_{TH} = 1$) we obtained a total of about 30,000 detections since almost all 80 TDCs got triggered. As can be seen, the signal-to-background ratio is clearly improved when only SPADs inside the laser spot are allowed to trigger the shared TDCs, thus validating the proposed smart ROI detection approach.
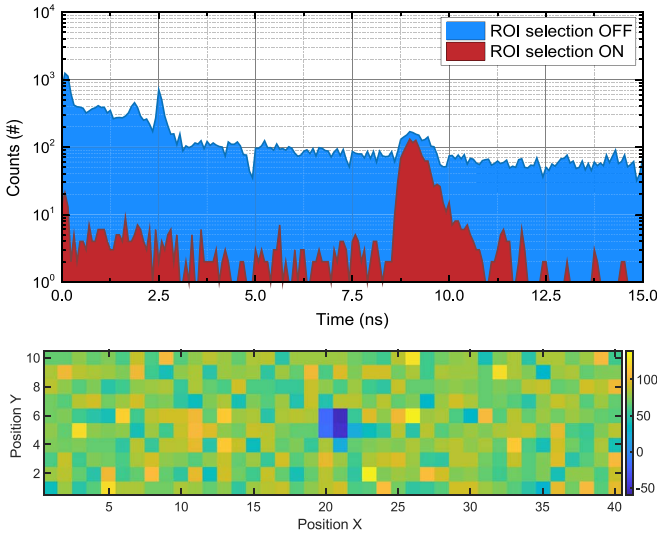
FIGURE 14. Comparison (top) between TOF histograms acquired with ROI detection on and off and counts map (bottom) with $N_{TH} = 80$ and 2.2 klux background light.
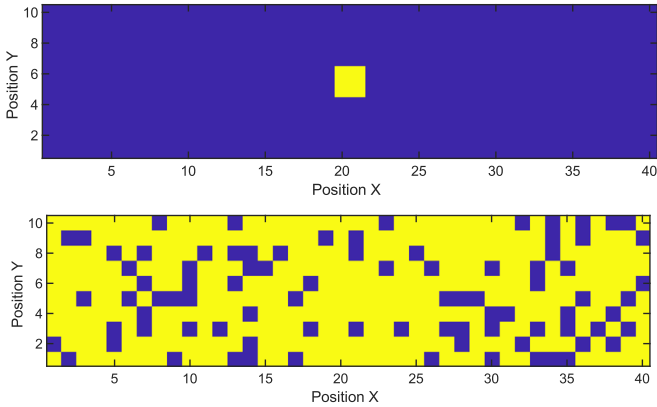

FIGURE 15. ROI detection map with $N_{TH} = 80$ (top) and with $N_{TH} = 1$ (bottom) at 2.2 klux background light.

FIGURE 16. Temporal response of single SPAD pixel ROI (top) and 12 SPAD pixels (bottom) within the ROI.
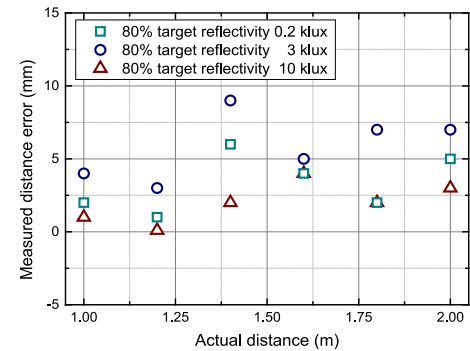
FIGURE 17. Measured distance error, at different background levels.

C. TOF MEASUREMENTS

Once the laser spot is located within the array through the on-chip smart ROI detection, TOF measurements can be performed. We employed the optical setup showed in Fig. 9. The single-photon timing precision of the whole SPAD-to-TDC chain is shown in Fig. 16, when using a 670 nm pulsed laser (300 ps FWHM): the 390 ps FWHM response of a single SPAD increases to 468 ps when 12 SPADs are enabled by the ROI detection circuitry. This variation is mainly due to timing skews between TDCs (see Fig. 12) and between SPADs along each row (see Section II-C). However, even if the single-shot precision is deteriorated, the final precision obtained from the centroid computation is nevertheless improved due to the more TOF samples which are obtained with the 12 SPADs enabled by the ROI detection logic.

Note that the ROI consists of just 12 SPADs and is much smaller than the nominal one, reported in [21]. This is due to the optical setup and employed laser, which was unable to guarantee a homogeneous spot, resulting in a much smaller
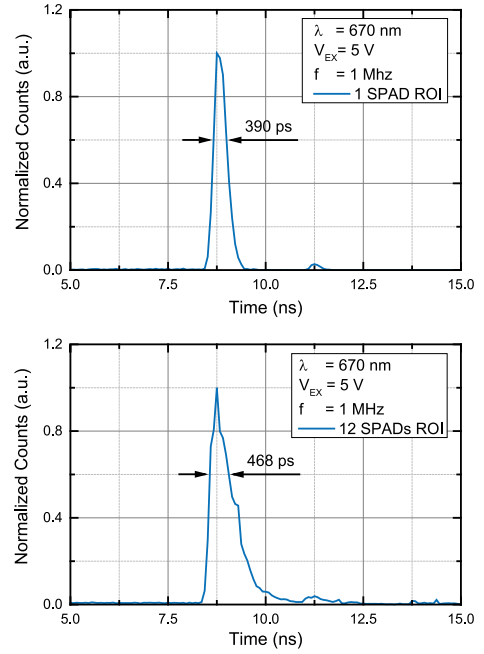
ROI detection area and also the ROI detection area varies as the background and threshold change in the various measurements.

Fig. 17 shows the measured distance error vs. the actual distance across the whole 2 m range, at different background levels (up to 10 klux from the halogen lamp), whereas Fig. 18 shows the distance precision at different measured distances within the FSR and background levels. The results reported in Fig. 17 and Fig. 18 are obtained with 12 SPAD pixels enabled by the ROI detection, with 500 laser shots at 1 MHz repetition rate, reaching 2 kHz (i.e., 0.5 ms) measurements rate and off-chip histograms centroid computation. Measurements were performed up to 2 m with an achieved precision of about 2.3 mm at 1 m distance with 80% target reflectivity and 3 klux background light, while accuracy (i.e., deviation from the real distance) is lower than 10 mm across the whole FSR. At 10 klux, the precision is worsened to 20 mm at 2 m distance.
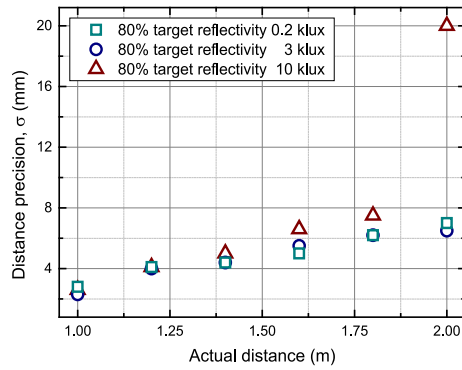
FIGURE 18. Distance precision up to 2 m distance, at different background levels.
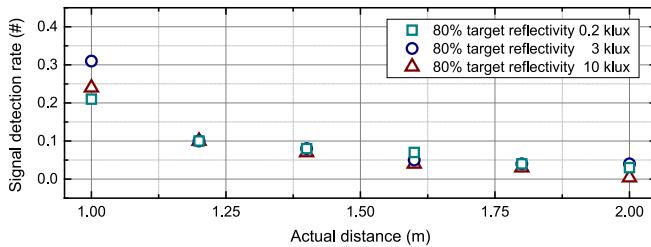

FIGURE 19. Signal detection rate for measurements performed at different distance.
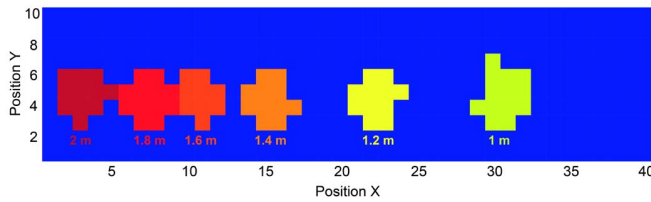

FIGURE 20. ROI detection map at different distance measurements.

TABLE 2. Comparison with state-of-the-art rangefinder system based on SPAD array.

Ref.	This work	[12]	[14]
Receiver characteristics			
Technology	160 nm	150 nm	350 nm HV
Approach	ROI detection	ROI detection	Time-gating
Array size	40×10	50×40	9×9
Fill Factor	14%	15.3 %	50%
No. TDC	80	25	10
TDC LSB	78 ps	40.7 ps	65 ps
Range	2.2 m	7.5 m	80 m
Power (chip)	220 mW	28.3 mW	-
Emitter parameters			
Wavelength	670 nm	470 nm	810 nm
Power (avg)	14 µW	40 µW	50 µW
Pulse width (FWHM)	300 ps	150 ps	100 ps
Repetition rate	1 MHz	10 MHz	100 kHz
Optics parameters			
Lens focal length	12 mm	-	40 mm
Lens aperture	8.57 mm	-	20 mm
Optical filter bandwidth	10 nm (band-pass)	50 nm (band-pass)	50 nm (band-pass)
Ranging performance			
Target reflectivity	80%	90%	11%
Meas. rate	2 kHz	1 kHz	0.17 Hz
Maximum range (measured)	2 m	3 m	73.2 m
Maximum background	10 klux	18 klux	90 klux
Accuracy	< 10 mm	< 19 mm	< 0.5 mm
Dist. precision (Background)	< 2.3 mm (1σ) 3 klux	< 1.6 mm (1σ) 7 klux	< 20 mm (FWHM) 50 lux

Fig. 19 shows the signal detection rate (i.e., the average number of TOF detections at each laser shot) at various distance and background conditions for the distance measurements of Fig. 17 and Fig. 18. As shown in Fig. 19, the signal detection rate is low compared to the desired value reported in [21], again due to the non-homogeneous laser spot and the optical setup used, resulting in a much smaller ROI which significantly reduces the total number of detections per frame.

Fig. 20 shows the ROI map positions at different distances of the target (see Fig. 17 and Fig. 18). As shown in Fig. 20, due to the triangulation between emitter and receiver, distances shorter than 1 m cannot be performed since the laser spot come out of the SPAD array.

The overall average power consumption of the chip is about 220 mW, including both the SPAD array and the core circuitry. The main contribution comes from the buffers used to distribute the multiphase clocks to the 80 TDCs and the DLL used to generate the multiphase clocks for TDC interpolators. Table 2 compares the performance of state-of-the-art rangefinder systems based on SPAD arrays. As can be seen, the precision of our chip is good, obtaining about 2.3 mm

at 3 klux background light, even with high measurement rate and low laser power. Also, the accuracy is good, lower than 10 mm and the maximum background is about 10 klux, limited by the halogen lamp used for the measurement.

IV. CONCLUSION
In this work we proposed a novel architecture for a single-point range-finding sensor, based on an array of 40 × 10 SPAD detectors, which employs a smart Region-of-Interest detection circuitry to identify the few SPADs hit by the signal photons among the many others hit by the stronger ambient light background. 80 shared TDCs among the 400 SPADs allow to reduce power consumption and improve SNR and precision of distance measurements. The experimental results show that the chip guarantees a precision better than 2.3 mm (80% target reflectivity) at 2 m distance with 3 klux background light and lower than 20 mm at 10 klux at 2 m distance. The device is tailored for

high precision distance measurements in short-range applications in industrial environments, where background ambient illumination is dominant.

Some challenges need to be addressed to extend the proposed design to longer distances (e.g., up to 100 m). For instance, it will be necessary to increase the number of pixels along the horizontal dimension in order to cover the wider displacement occurring at longer distances due to the non-confocal setup. Consequently, more SPADs will share the same TDC, hence the time skew between different SPADs will increase, thus impacting more and more the distance precision.

REFERENCES

[1] M. E. Warren, "Automotive LIDAR technology," in *Proc. Symp. VLSI Circuits*, Kyoto, Japan, 2019, pp. C254–C255.

[2] Y. Li and J. Ibanez-Guzman, "Lidar for autonomous driving: The principles, challenges, and trends for automotive Lidar and perception systems," *IEEE Signal Process. Mag.*, vol. 37, no. 4, pp. 50–61, Jul. 2020.

[3] P. Sudhakar, K. A. Sheel, and M. Satyanarayana, "Imaging Lidar system for night vision and surveillance applications," in *Proc. 4th Int. Conf. Adv. Comput. Commun. Syst. (ICACCS)*, Coimbatore, India, 2017, pp. 1–6.

[4] C. Steger, M. Ulrich, and C. Wiedemann, *Machine Vision Algorithms and Applications*. Hoboken, NJ, USA: Wiley, 2018.

[5] A. W. Yu *et al.*, "Orbiting and in-situ Lidars for earth and planetary applications," in *Proc. IEEE Int. Geosci. Remote Sens. Symp. (IGARSS)*, 2020, pp. 3479–3482.

[6] D. Bronzi, F. Villa, S. Tisa, A. Tosi, and F. Zappa, "SPAD figures of merit for photon-counting, photon-timing, and imaging applications: A review," *IEEE Sensors J.*, vol. 16, no. 1, pp. 3–12, Jan. 2016.

[7] F. Villa, F. Severini, F. Madonini, and F. Zappa, "SPADs and SiPMs arrays for long-range high-speed light detection and ranging (LiDAR)," *Sensors*, vol. 21, no. 11, p. 3839, Jun. 2021.

[8] W. Becker, *Advanced Time-Correlated Single Photon Counting Techniques*. Berlin, Germany: Springer-Verlag, 2005.

[9] S. Pellegrini, G. S. Buller, J. M. Smith, A. M. Wallace, and S. Cova, "Laser-based distance measurement using picosecond resolution time-correlated single-photon counting," *Meas. Sci. Technol.*, vol. 11, no. 6, pp. 712–716, 2000.

[10] J. S. Massa, A. M. Wallace, G. S. Buller, S. J. Fancey, and A. C. Walker, "Laser depth measurement based on time-correlated single-photon counting," *Opt. Lett.*, vol. 22, no. 8, pp. 543–545, 1997.

[11] N. A. W. Dutton *et al.*, "11.5 a time-correlated single-photon-counting sensor with 14GS/S histogramming time-to-digital converter," in *IEEE Int. Solid-State Circuits Conf. (ISSCC) Dig. Tech. Papers*, San Francisco, CA, USA, 2015, pp. 1–3.

[12] M. Perenzoni, N. Massari, L. Gasparini, M. M. Garcia, D. Perenzoni, and D. Stoppa, "A fast 50 × 40-pixels single-point DTOF SPAD sensor with photon counting and programmable ROI TDCs, with σ <4 mm at 3 m up to 18 klux of background light," *IEEE Solid-State Circuits Lett.*, vol. 3, pp. 86–89, 2020.

[13] C. Zhang, S. Lindner, I. M. Antolović, J. M. Pavia, M. Wolf, and E. Charbon, "A 30-frames/s, 252×144 SPAD flash LiDAR with 1728 dual-clock 48.8-ps TDCs, and pixel-wise integrated histogramming," *IEEE J. Solid-State Circuits*, vol. 54, no. 4, pp. 1137–1151, Apr. 2019.

[14] J. Huikari, S. Jahromi, J.-P. Jansson, and J. Kostamovaara, "Compact laser radar based on a subnanosecond laser diode transmitter and a two-dimensional CMOS single-photon receiver," *Opt. Eng.*, vol. 57, no. 2, 2018, Art. no. 024104.

[15] M. Perenzoni, D. Perenzoni, and D. Stoppa, "A 64×64-pixels digital silicon photomultiplier direct TOF sensor with 100-mphotons/s/pixel background rejection and imaging/altimeter mode with 0.14% precision up to 6 km for spacecraft navigation and landing," *IEEE J. Solid-State Circuits*, vol. 52, no. 1, pp. 151–160, Jan. 2017.

[16] M. Beer, J. F. Haase, J. Ruskowski, and R. Kokozinski, "Background light rejection in SPAD-based LiDAR sensors by adaptive photon coincidence detection," *Sensors*, vol. 18, no. 12, p. 4338, Dec. 2018.

[17] C. Niclass, M. Soga, H. Matsubara, S. Kato, and M. Kagami, "A 100-m range 10-frame/s 340×96-pixel time-of-flight depth sensor in 0.18-μm CMOS," *IEEE J. Solid-State Circuits*, vol. 48, no. 2, pp. 559–572, Feb. 2013.

[18] P. Padmanabhan *et al.*, "7.4 A 256×128 3D-stacked (45nm) SPAD FLASH LiDAR with 7-level coincidence detection and progressive gating for 100m range and 10klux background light," in *Proc. IEEE Int. Solid-State Circuits Conf. (ISSCC)*, 2021, pp. 111–113.

[19] R. K. Henderson *et al.*, "5.7 A 256×256 40nm/90nm CMOS 3D-stacked 120dB dynamic-range reconfigurable time-resolved SPAD imager," in *Proc. IEEE Int. Solid-State Circuits Conf. (ISSCC)*, 2019, pp. 106–108.

[20] J. Kostamovaara, S. S. Jahromi, and P. Keränen, "Temporal and spatial focusing in SPAD-based solid-state pulsed time-of-flight laser range imaging," *Sensors*, vol. 20, no. 21, p. 5973, Oct. 2020.

[21] V. Sesta *et al.*, "Spot tracking and TDC sharing in SPAD arrays for TOF LiDAR," *Sensors*, vol. 21, no. 9, p. 2936, Apr. 2021.

[22] S. P. Namboodiri, G. Arteaga, J. Skelly, F. Mata-Carlos, A. Roy, and R. J. Baker, "A current-mode photon counting circuit for long-range LiDAR applications," in *Proc. IEEE 63rd Int. Midwest Symp. Circuits Syst. (MWSCAS)*, Springfield, MA, USA, 2020, pp. 146–149.

[23] A. Eshkoli and Y. Nemirovsky, "Characterization and architecture of monolithic N*P-CMOS-SiPM array for ToF measurements," *IEEE Trans. Instrum. Meas.*, vol. 70, pp. 1–9, Dec. 2021.

[24] F. Arvani, T. C. Carusone, and E. S. Rogers, "TDC sharing in SPAD-based direct time-of-flight 3D imaging applications," in *Proc. IEEE Int. Symp. Circuits Syst. (ISCAS)*, Sapporo, Japan, 2019, pp. 1–5.

[25] C. Zhang, S. Lindner, I. M. Antolovic, M. Wolf, and E. Charbon, "A CMOS SPAD imager with collision detection and 128 dynamically reallocating TDCs for single-photon counting and 3D time-of-flight imaging," *Sensors*, vol. 18, no. 11, p. 4016, Nov. 2018.

[26] M. Sanzaro, P. Gattari, F. Villa, A. Tosi, G. Croce, and F. Zappa, "Single-photon avalanche diodes in a 0.16 μm BCD technology with sharp timing response and red-enhanced sensitivity," *IEEE J. Sel. Topics Quantum Electron.*, vol. 24, no. 2, pp. 1–9, Mar./Apr. 2018.

[27] D. Bronzi, S. Tisa, F. Villa, S. Bellisai, A. Tosi, and F. Zappa, "Fast sensing and quenching of CMOS SPADs for minimal afterpulsing effects," *IEEE Photon. Technol. Lett.*, vol. 25, no. 8, pp. 776–779, Apr. 15, 2013.

[28] D. Portaluppi, E. Conca, and F. Villa, "32 × 32 CMOS SPAD imager for gated imaging, photon timing, and photon coincidence," *IEEE J. Sel. Topics Quantum Electron.*, vol. 24, no. 2, pp. 1–6, Mar./Apr. 2018.

[29] V. Sesta, F. Villa, E. Conca, and A. Tosi, "A novel sub-10 ps resolution TDC for CMOS SPAD array," in *Proc. 25th IEEE Int. Conf. Electron. Circuits Syst. (ICECS)*, Bordeaux, France, 2018, pp. 5–8.

[30] R. Sumner, "A sliding scale method to reduce the differential non linearity of a time digitizer," in *Proc. IEEE Nucl. Sci. Symp. Conf. Rec.*, vol. 2. San Diego, CA, USA, 2001, pp. 803–806.

VINCENZO SESTA was born in Ribera, Italy, in 1991. He received the master's degree in electronics engineering and the Ph.D. degree in information technology from the Politecnico di Milano, Milan, Italy, in 2016 and 2020, respectively, where he is currently a Postdoctoral Researcher with the Department of Electronics, Information and Bioengineering. His research activity focuses on the design and development of time-to-digital converters and timing electronics CMOS circuits for arrays of silicon SPADs.

KLAUS PASQUINELLI was born in Seriate, Italy, in 1994. He received the bachelor's and M.Sc. degrees in electronics engineering from the Politecnico di Milano in 2016 and October 2018, respectively, where he is currently pursuing the Ph.D. degree in information technology. His research interests include the design, development, and testing of systems with single-photon avalanche diodes matrices and digital silicon photomultiplier.

RENATO FEDERICO was born in Como, Italy, in 1994. He received the master's degree in electronics engineering from the Politecnico di Milano, Milan, Italy, in 2019. Since October 2019, he has been working as a Flash Memory Analog Designer with SK Hynix Italy S.r.l, Agrate Brianza, Italy.

FRANCO ZAPPA (Senior Member, IEEE) was born in Milano, Italy, in 1965. He received the M.S.E.E. and Ph.D. degrees from the Politecnico di Milano in 1989 and 1993, respectively, where he has been a Full Professor of Electronics since 2011. He cofounded "Micro Photon Devices" (SPAD modules and cameras for single photon-counting and photon-timing) and "pioNIRS" (compact instrumentation for time-domain Near-Infrared Spectroscopy TD-NIRS of materials and tissues, e.g., for continuous monitoring of brain and muscle activities). He has coauthored more than 250 papers, published in peer-reviewed journals and in conference proceedings, and eight textbooks on *Electronic Design, Electronic Systems, and Microcontrollers*. His research focuses on microelectronics for CMOS and BCD SPAD imagers, for high-sensitivity time-resolved optical measurements, 2D imaging, and 3D depth ranging via single-photons' time-of-flight.

FEDERICA VILLA (Member, IEEE) was born in Milano, Italy, in 1986. She received the B.Sc. degree in biomedical engineering, the M.Sc. degree (*summa cum laude*) in electronic engineering, and the Ph.D. degree in information and communication technology from the Politecnico di Milano in 2008, 2010, and 2014, respectively, where she has been an Assistant Professor since 2015. She has coauthored about 130 papers. Her current research activities include the design and development of CMOS SPAD imagers for 2D imaging via single-photon counting and 3D ranging through direct time-of-flight photon-timing.